
FAITHFUL SYNTHESIS OF LOW-DOSE CONTRAST-ENHANCED BRAIN MRI SCANS USING NOISE-PRESERVING CONDITIONAL GANS

A PREPRINT

 **Thomas Pinetz***

Institute of Applied Mathematics
University of Bonn
pinetz@iam.uni-bonn.de

 **Erich Kobler**

Department of Neuroradiology
University Medical Center Bonn
erich.kobler@ukbonn.de

 **Robert Haase**

Department of Neuroradiology
University Medical Center Bonn
robert.haase@ukbonn.de

 **Katerina Deike-Hofmann**

Department of Neuroradiology
University Medical Center Bonn
katerina.deike-hofmann@ukbonn.de

 **Alexander Radbruch**

Department of Neuroradiology
University Medical Center Bonn
alexander.radbruch@ukbonn.de

Alexander Effland

Institute of Applied Mathematics
University of Bonn
effland@iam.uni-bonn.de

ABSTRACT

Today Gadolinium-based contrast agents (GBCA) are indispensable in Magnetic Resonance Imaging (MRI) for diagnosing various diseases. However, GBCAs are expensive and may accumulate in patients with potential side effects, thus dose-reduction is recommended. Still, it is unclear to which extent the GBCA dose can be reduced while preserving the diagnostic value – especially in pathological regions. To address this issue, we collected brain MRI scans at numerous non-standard GBCA dosages and developed a conditional GAN model for synthesizing corresponding images at fractional dose levels. Along with the adversarial loss, we advocate a novel content loss function based on the Wasserstein distance of locally paired patch statistics for the faithful preservation of noise. Our numerical experiments show that conditional GANs are suitable for generating images at different GBCA dose levels and can be used to augment datasets for virtual contrast models. Moreover, our model can be transferred to openly available datasets such as BraTS, where non-standard GBCA dosage images do not exist. Code is available here.

Keywords MRI, GANs, Optimal Transport, Noise Modelling

1 Introduction

Magnetic Resonance Imaging (MRI) of the brain is an essential imaging modality to accurately diagnose various neurological diseases ranging from inflammatory lesions to brain tumors and metastases. For accurate depictions of said pathologies, gadolinium-based contrast agents (GBCA) are injected intravenously to highlight brain-blood barrier dysfunctions. However, these contrast agents are expensive and may cause nephrogenic systemic fibrosis in patients with severely reduced kidney function [32]. Moreover, [18] reported that Gadolinium accumulates inside patients with unclear health consequences, especially after repeated application. The American College of Radiology recommends administering the lowest GBCA dose to obtain the needed clinical information [1].

Driven by this recommendation, several research groups have recently published dose-reduction techniques focusing on maintaining image quality. Complementary to the development of higher relaxivity contrast agents [29], virtual contrast [9, 3] – replacing a large fraction of the GBCA dose by deep learning – has been proposed. These approaches typically acquire a contrast-enhanced (CE) scan with a lower GBCA dose along with non-CE scans, e.g., T1w, T2w, FLAIR, or ADC. These input images are then processed by a deep neural network (DNN) to replicate the correspond-

*Thomas Pinetz and Erich Kobler contributed equally to this work.

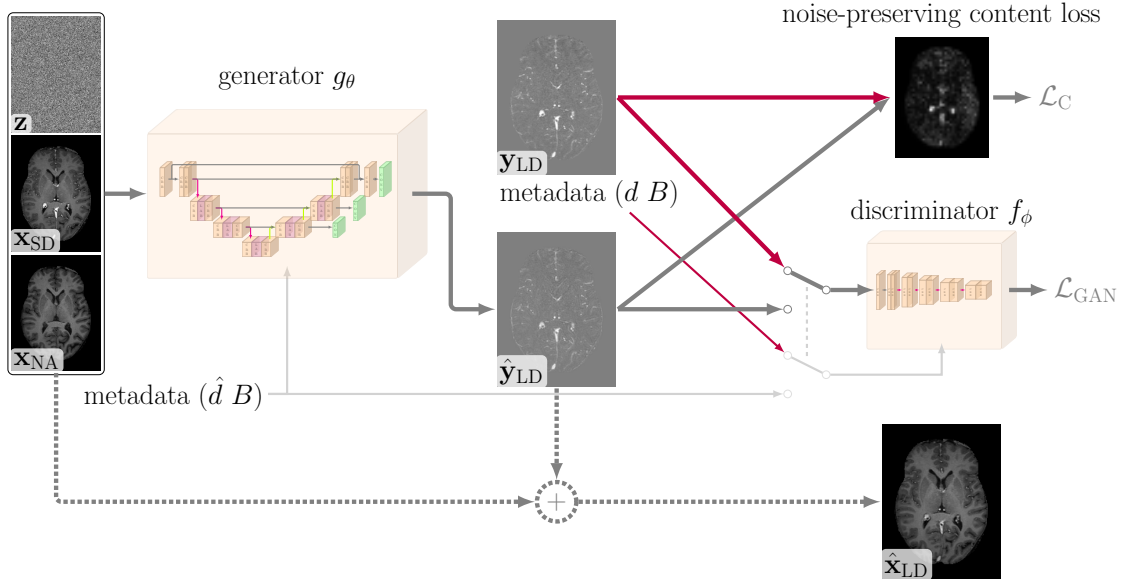


Figure 1: Low-dose synthesis using a conditional GAN. The generator predicts a residual low-dose image \hat{y}_{LD} from a noise sample z conditioned on the native x_{NA} and standard-dose x_{SD} images as well as the field strength B and the artificial dose \hat{d} . Along with the discriminator, a novel noise-preserving loss – penalizing the Wasserstein distance of paired patches – is used for training. At inference, the generated residual \hat{y}_{LD} is added to the native image x_{NA} to yield the corresponding synthetic low-dose \hat{x}_{LD} .

ing standard-dose scan. While promising, virtual contrast techniques have not been integrated into clinical practice yet due to false-positive signals or missed small lesions [24, 3]. As with all deep learning-based approaches, the availability of large datasets is essential, which is problematic in the considered case since the additional CE low-dose scan is not acquired in clinical routine exams. Hence, there are no public datasets to easily benchmark and compare different algorithms or evaluate their performance. In general, the enhancement behavior of pathological tissues at various GBCA dosages has barely been researched due to a lack of data [13].

In recent years, generative models have been used to overcome data scarcity in the computer vision and medical imaging community. Frequently, generative adversarial networks (GANs) [10] are applied as state-of-the-art in image generation [31] or semantic translation/interpolation [19, 6, 22]. In a nutshell, the GAN framework trains two competing DNNs – the generator and the discriminator. The generator learns a non-linear transformation of a predefined noise distribution to fit the distribution of a target dataset, while the discriminator provides feedback by simultaneously approximating a distance or divergence between the generated and the target distribution. The choice of this distance leads to the well-known different GAN algorithms, e.g., Wasserstein GANs [4, 11], Least Squares GANs [25], or Non-saturating GANs [10]. However, Lucic et al. [23] showed that this choice has only a minor impact on the performance.

Learning conditional distributions between images can be accomplished by additionally feeding a condition (additional scans, dose level, etc.) into both the generator and discriminator. In particular, for image-to-image translation tasks, these conditional GANs have been successfully applied using paired [15, 26, 28] and unpaired training data [36]. Within these methods, an additional content (cycle) loss typically penalizes pixel-wise deviations (e.g., ℓ_1) from a corresponding reference to enforce structural similarity, whereas a local adversarial loss (discriminator with local receptive field) controls textural similarity. In addition, embeddings have been used to inject metadata [19, 8].

To study the GBCA accumulation behavior, we collected 453 CE scans with non-standard GBCA doses in the set of $\{10\%, 20\%, 33\%\}$ along with the corresponding standard-dose (0.1 mmol/kg) scan after applying the remaining contrast agent. Using this dataset, we aim at the semantic interpolation of the GBCA signal at various fractional dose levels. To this end, we use GANs to learn the contrast enhancement behavior from the dataset collective and thereby enable the synthesis of contrast signals at various dose levels for individual cases. Further, to minimize the smoothing effect [20] of typical content losses (e.g., ℓ_1 or perceptual [17]), we develop a noise-preserving content loss function based on the Wasserstein distance between paired image patches calculated using a Sinkhorn-style algorithm. This

novel loss enables a faithful generation of noise, which is important for the identification of enhancing pathologies and their usability as additional training data.

With this in mind, the contributions of this work are as follows:

- synthesis of GBCA behavior at various doses using conditional GANs,
- loss enabling interpolation of dose levels present in training data,
- noise-preserving content loss function to generate realistic synthetic images.

2 Methodology

Given a *native* image \mathbf{x}_{NA} (i.e. without any contrast agent injection) and a CE *standard-dose* image \mathbf{x}_{SD} , our conditional GAN approach synthesizes CE *low-dose* images $\hat{\mathbf{x}}_{\text{LD}}$ for selected dose levels $\hat{d} \in \mathcal{D} \subset [0, 1]$ from a uniform noise image $\mathbf{z} \sim \mathcal{N}(0, \text{Id})$, see Figure 1. To focus the generation on the contrast agent signal, our model predicts residual images $\hat{\mathbf{y}}_{\text{LD}}$; the corresponding low-dose can be obtained by $\hat{\mathbf{x}}_{\text{LD}} = \mathbf{x}_{\text{NA}} + \hat{\mathbf{y}}_{\text{LD}}$.

For training and evaluation, we consider samples $(\mathbf{x}_{\text{NA}}, \mathbf{x}_{\text{SD}}, \mathbf{y}_{\text{LD}}, d, B)$ of a dataset DS , where $\mathbf{y}_{\text{LD}} = \mathbf{x}_{\text{LD}} - \mathbf{x}_{\text{NA}}$ is the residual image of a real CE low-dose scan \mathbf{x}_{LD} with dose level $d \in \mathcal{D}$ and $B \in \{1.5, 3\}$ is the field-strength in Tesla of the used scanner. To simplify learning of the contrast accumulation behavior, we adapt the preprocessing pipeline of BraTS [37]. Further details of the dataset and the preprocessing are in the supplementary material.

2.1 Conditional GANs for Contrast Signal Synthesis

Our approach is built on the insight that contrast enhancement is an inherently local phenomenon and the necessary information for the synthesis task can be extracted from a local neighborhood within an image. Therefore, we use as generator g_θ a convolutional neural network (CNN) that is based on the U-Net [30] along with a local attention mechanism. The architecture design and the implementation details can be found in the supplementary material. As illustrated in Figure 1, the generator uses a 3D noise sample $\mathbf{z} \sim \mathcal{N}(0, \text{Id})$ along with the native and SD images $(\mathbf{x}_{\text{NA}}, \mathbf{x}_{\text{SD}})$ as input. The synthesis is guided by the metadata $(\hat{d} B)^\top$, containing the artificial dose level $\hat{d} \in \mathcal{D}$ as well as the field strength of the corresponding scanner $B \in \{1.5, 3\}$. In particular, the metadata is injected into every residual block of the generator using an embedding, motivated by the recent success of diffusion-based models [14].

To learn this generator, a convolutional discriminator f_ϕ is used, which is in turn trained to distinguish the generated residual images $\hat{\mathbf{y}}_{\text{LD}}$ with random dose level \hat{d} from the real residual images \mathbf{y}_{LD} with the associated real dose level d . To make this a non-trivial task, label smoothing on the metadata is used, i.e. the real dose is augmented by zero-mean additive Gaussian noise with standard deviation 0.05. The discriminator architecture essentially implements the encoding side of the generator, however, no local attention layers are used as suggested by [21]. Like the generator, the discriminator is conditioned on the metadata using an embedding, which is not shared between both networks.

For training of the generator θ and discriminator ϕ , we consider the loss

$$\min_{\theta} \max_{\phi} \{ \mathcal{L}_{\text{GAN}}(\theta, \phi) + \lambda_{\text{GP}} \mathcal{L}_{\text{GP}}(\phi) + \lambda_{\text{C}} \mathcal{L}_{\text{C}}(\theta) \}, \quad (1)$$

which consists of a Wasserstein GAN loss \mathcal{L}_{GAN} , a gradient penalty loss \mathcal{L}_{GP} , and a content loss \mathcal{L}_{C} that are relatively weighted by scalar non-negative factors λ_{GP} and λ_{C} . In detail, the Wasserstein GAN loss reads as

$$\mathcal{L}_{\text{GAN}}(\theta, \phi) := \mathbb{E}_{(\mathbf{x}_{\text{NA}}, \mathbf{x}_{\text{SD}}, \mathbf{y}_{\text{LD}}, d, B) \sim \mathcal{U}(\text{DS})} \left\{ f_\phi(\mathbf{y}_{\text{LD}}, c) - \mathbb{E}_{\mathbf{z} \sim \mathcal{N}(0, \text{Id}), \hat{d} \sim \mathcal{U}(\mathcal{D})} \left\{ f_\phi(g_\theta(\mathbf{z}, \hat{c}), \hat{c}) \right\} \right\}$$

using condition tuples $c = (\mathbf{x}_{\text{NA}}, \mathbf{x}_{\text{SD}}, (d B)^\top)$ and $\hat{c} = (\mathbf{x}_{\text{NA}}, \mathbf{x}_{\text{SD}}, (\hat{d} B)^\top)$ to simplify notation. $\mathcal{U}(\mathcal{S})$ denotes a uniform distribution over a set \mathcal{S} . We highlight that the artificial dose levels \hat{d} for the generated images are uniformly sampled from $\mathcal{D} = [0.05, 0.5]$, which enables an interpolation around the dose levels present in the dataset DS . This is necessary since only a few distinct dose levels $\{0.1, 0.2, 0.33\}$ have been acquired. For regularizing the discriminator f_ϕ , we include the gradient penalty loss

$$\mathcal{L}_{\text{GP}}(\phi) := \mathbb{E}_{(\mathbf{x}_{\text{NA}}, \mathbf{x}_{\text{SD}}, \mathbf{y}_{\text{LD}}, d, B) \sim \mathcal{U}(\text{DS})} \left\{ (\|\nabla f_\phi(h(\alpha, \mathbf{y}_{\text{LD}}, \hat{\mathbf{y}}_{\text{LD}}), h(\alpha, c, \hat{c}))\|_2 - 1)^2 \right\}$$

$$\mathbf{z} \sim \mathcal{N}(0, \text{Id}), \hat{d} \sim \mathcal{U}(\mathcal{D}), \alpha \sim \mathcal{U}(0, 1)$$

using $h(\alpha, \mathbf{y}, \hat{\mathbf{y}}) = \alpha \hat{\mathbf{y}} + (1 - \alpha) \mathbf{y}$. A penalty term is introduced, if f_ϕ is not Lipschitz continuous with factor 1 in its arguments as required by Wasserstein GANs [11]. Here, $\hat{\mathbf{y}}_{\text{LD}} = g_\theta(\mathbf{z}, \hat{c})$ and the Lipschitz penalty is evaluated

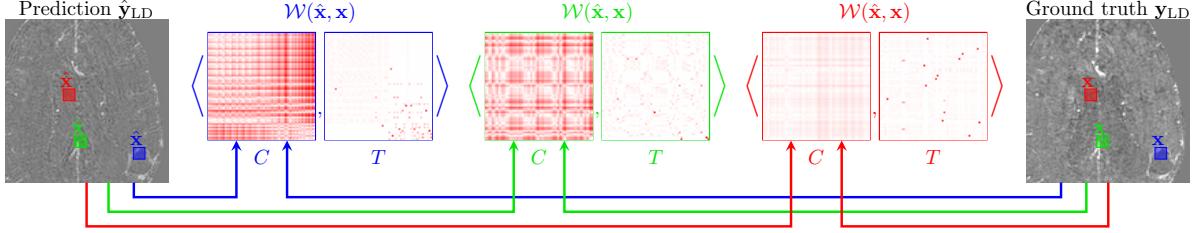


Figure 2: Illustration of our patch-wise noise-preserving content loss. For each patch pair $((\hat{\mathbf{x}}, \mathbf{x}), (\hat{\mathbf{x}}, \mathbf{x}), (\hat{\mathbf{x}}, \mathbf{x}))$ extracted at the same position, the loss accounts for the Wasserstein distance \mathcal{W} of the associated empirical distributions. In the center, the corresponding cost matrices C (pixel-wise absolute difference) along with the optimal transport maps T are shown, which are obtained by solving (2). The final loss is the sum of the element-wise multiplication of all C and T for every non-overlapping patch.

at convex combinations of real and synthetic images and condition tuples (essentially dose levels). Finally, using a distance ℓ_C , the content loss

$$\mathcal{L}_C(\theta) := E_{(\mathbf{x}_{NA}, \mathbf{x}_{SD}, \mathbf{y}_{LD}, d, B) \sim \mathcal{U}(\text{DS}), \mathbf{z} \sim \mathcal{N}(0, \text{Id})} \{ \ell_C(g_\theta(\mathbf{z}, c), \mathbf{y}_{LD}) \}$$

guides the generator g_θ towards residual images in the dataset. Thus, it teaches the generator the principles of contrast enhancement. Typically, the ℓ_1 -norm is used as a distance function, which leads to smooth results since it also penalizes deviations from the noise in y_{LD} .

2.2 Noise-preserving Content Loss

To generate realistic CE images, it is also important to retain the original noise characteristics. Therefore, we introduce a novel loss that accounts for deviations in local statistics using optimal transport between empirical distributions of paired patches, as illustrated in Figure 2.

Let $\mathbf{x}, \hat{\mathbf{x}} \in \mathbb{R}^{n^3}$ be patches of size $n \times n \times n$ extracted from the same location of a real and synthetic image, respectively. The Wasserstein distance of the associated empirical distributions using a transport plan $T \in \mathbb{R}_+^{n^3 \times n^3}$ and cost matrix $C \in \mathbb{R}_+^{n^3 \times n^3}$ given by $(C_{ij} = |\hat{x}_i - x_j|)$ is defined as

$$\mathcal{W}(\hat{\mathbf{x}}, \mathbf{x}) = \min_{T \in \mathbb{R}_+^{n^3 \times n^3}} \langle C, T \rangle_F \quad \text{s.t.} \quad T\mathbf{1} = \mathbf{1} \frac{1}{n^3}, \quad T^\top \mathbf{1} = \mathbf{1} \frac{1}{n^3}, \quad (2)$$

where $\mathbf{1}$ is the vector of ones of size n^3 . In contrast to the element-wise difference penalization of the ℓ_1 -distance, the Wasserstein distance accounts for mismatches between distributions. To illustrate this, let us, for instance, assume that both patches are Gaussian distributed ($x \sim \mathcal{N}(\mu, \sigma)$, $\hat{x} \sim \mathcal{N}(\hat{\mu}, \hat{\sigma})$), which is a coarse simplification of real MRI noise [2]. In this case, the Wasserstein distance reduces to second-order momentum matching, i.e., $\mathcal{W}^2(\hat{\mathbf{x}}, \mathbf{x}) = (\mu - \hat{\mu})^2 + (\sigma - \hat{\sigma})^2$. Thus, the Wasserstein distance generalizes this distributional loss to any distribution within paired patches.

To efficiently solve problem (2), we use the inexact proximal point algorithm [35]. This algorithm is parallelized and applied to all non-overlapping patch pairs, to obtain our noise-preserving content loss

$$\ell_{\text{NP}}(\hat{\mathbf{y}}, \mathbf{y}) = \mathbb{E}_{\mathbf{o} \sim \mathcal{U}(\mathcal{O})} \left\{ \sum_{\mathbf{p} \in \mathcal{P}} \mathcal{W}(P_{\mathbf{p}+\mathbf{o}}\hat{\mathbf{y}}, P_{\mathbf{p}+\mathbf{o}}\mathbf{y}) \right\},$$

where $P_{\mathbf{p}}$ extracts a local $n \times n \times n$ patch at location $\mathbf{p} \in \mathcal{P} = \{0, n, 2n, \dots\}^3$ using periodic boundary conditions. Note that we compute the expectation over offsets $\mathbf{o} \in \mathcal{O} = \{0, 1, \dots, \lceil \frac{n}{2} \rceil\}^3$ to avoid patching artifacts. In the numerical implementation, only a single offset is sampled for time and memory constraints.

3 Numerical Results

In this section, we evaluate the proposed conditional GAN approach with a particular focus on different content loss distance functions. All synthesis models were trained on 250 samples acquired on 1.5T and 3T Philips Achieva scanners and evaluated on 193 test cases, all collected at site ①. Further details of the dataset, model and training can be found in the supplementary. In our experiments, we observed that the choice of the content loss distance

function $\ell_C(\hat{y}, y)$ strongly influences the performance. Thus, we consider the different cases:

$$\ell_1: \|\hat{y} - y\|_1 \quad \text{VGG: } \|h(\hat{y}) - h(y)\|_1 \quad \text{NP: } \ell_{\text{NP}}(\hat{y}, y)$$

Following Johnsen et al. [17], $h(x)$ is the VGG-16 model [33] up to relu3_3.

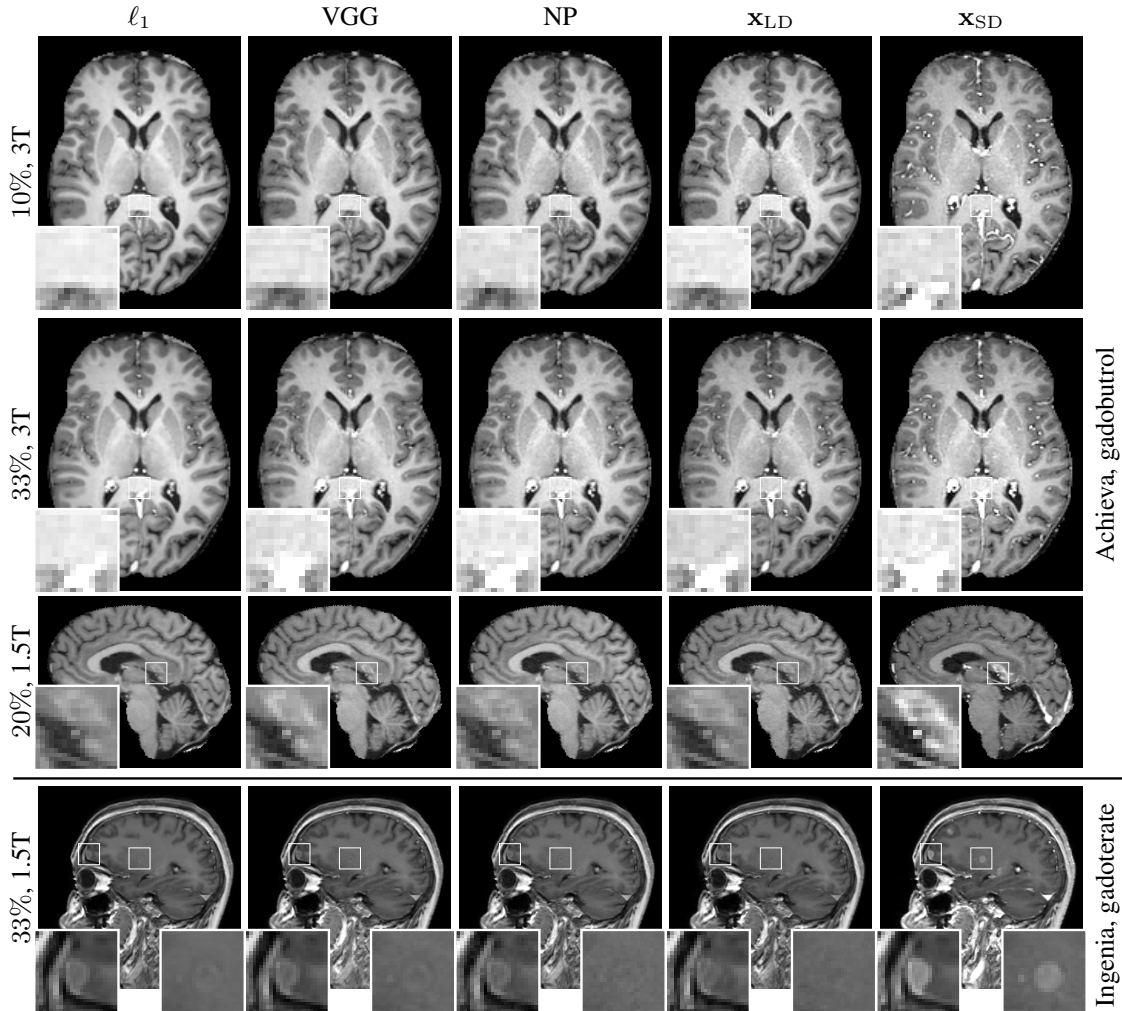


Figure 3: Qualitative comparison of synthesized images using different loss functions to the corresponding reference x_{LD} . While the ℓ_1 loss yields smooth low-dose images, the noise pattern is preserved to some extent using the VGG loss; our loss helps to further retain the noise characteristics.

A qualitative comparison of the different distance functions ℓ_C is visualized in Figure 3. The first column depicts synthesized images using the ℓ_1 -norm as the distance function. These images depict a plausible contrast signal, however, suffer from unrealistic smooth homogeneous regions. An improvement thereof is shown by the perceptual content loss (VGG). The NP-loss leads to a further improvement not only in the contrast signal behavior but also in the realism of the noise texture, cf. zoom regions in the lower corners.

To highlight the generalization capabilities, we depict in the bottom row of Figure 3 a sample from site ②, which was acquired using a Philips Ingenia scanner. Moreover, the GBCA gadoterate was used, while our training data only consists of scans using the GBCA gadobutrol. Nevertheless, all models present realistically synthesized LD images. Comparing the zooms of the LD images, we observe that our NP-loss leads to a better synthesis of noise and thereby to more realistic LD images. In the ℓ_1 and VGG columns, the noise is not faithfully synthesized, thus it is visually easy to spot the enhancing pathological regions.

For completeness, a quantitative ablation of the considered distance functions on the test images of site ① is shown in Table 1. Although neither maximizing PSNR nor SSIM [34] is our objective, we observe on-par performances of the perceptual (VGG) and our proposed content loss (NP) with the standard ℓ_1 distance function. Using the SD

Table 1: Quantitative comparison of the low-dose synthesis methods. The central columns present metrics evaluated on the synthesized low-dose images, whereas the right columns evaluate the effect of purely synthesized data for training the standard-dose prediction model [27]. Note, that the PSNR/SSIM of the standard dose prediction model was always evaluated on real LD images. The definitions of the mean absolute error on the contrast enhancement (MAE_{CE}) and on the noise standard deviation (MAE_{σ}) are in Section 3. A * denotes if a Wilcoxon signed rank test between VGG and $NP_{(our)}$ row is significant.

	low-dose synthesis				standard-dose prediction	
	PSNR	SSIM	MAE_{CE}	MAE_{σ}	PSNR	SSIM
ℓ_1	38.34	0.978	0.022	0.012	33.83	0.922
VGG	37.84	0.976	0.019	0.009	36.33	0.958
$NP_{(our)}$	38.05*	0.976	0.011*	0.004*	37.15*	0.960*
$x_{LD}^{(real)}$					39.07	0.974

image, we define CE pixels as those pixels at which the intensity increases by at least 10% compared to the native scan. An example of these CE regions is illustrated in the supplementary. Thus, the mean absolute error for CE pixels (MAE_{CE}) quantifies the enhancement behavior. Further, we estimate the standard deviation of the non-CE pixels and report the MAE to the ground truth standard deviation (MAE_{σ}). As shown in Table 1, our loss outperforms the other content losses to a large extent on both metrics, proving its effectiveness for faithful contrast enhancement and noise generation. Further statistical analyses are presented in the supplementary.

Next, we evaluate the effect of synthesized LD images on the performance of a virtual contrast model (VCM). In particular, we consider the state-of-the-art 2.5D U-Net model [27, 24, 12], which predicts an SD image given a corresponding native and LD image, see supplementary for further details. The columns on the right of Table 1 list the average PSNR and SSIM score on the *real* 33% LD subset of our test data from site ①. The bottom row depicts the performance if just *real* 33% LD images are used for training the VCM as an upper bound. In contrast, the other entries on the right list the performance if *only synthesized* LD images are used for training. Both metrics show that the samples synthesized using our NP-loss model are superior to both ℓ_1 and VGG.

To determine the effectiveness of the LD synthesis models at different settings, we acquired 160 data samples from 1.5T and 3T Philips Ingenia scanners at site ②. This site used the GBCA gadoterate, which has a lower relaxivity compared to gadobutrol used at site ① [16]. For 80 samples real LD images were acquired, which are used for testing. Using the VCM solely trained on the real 33% LD data of site ① yields an average PSNR and MAE_{CE} on the test samples of site ② of 40.04 and 0.092, respectively. Extending the training data for the VCM by synthesized LD images from our model with NP-loss, we get a significantly improved ($p < 0.001$) PSNR score of 40.37 and MAE_{CE} of 0.075.

Finally, Figure 4 visualizes synthesized LD images on the BraTS dataset [37] along with the associated VCM outputs. Comparing the predicted SD images \hat{x}_{SD} using 10% and 33% synthesized LD images \hat{x}_{LD} , we observe that the weakly enhancing tumor at the bottom zoom is not preserved in the case of 10%, enabling evaluation of dose reduction methods on known pathological regions.

4 Conclusions

In this work, we used conditional GANs to synthesize contrast-enhanced images using non-standard GBCA doses. To this end, we introduced a novel noise-preserving content loss motivated by optimal transport theory. Numerous numerical experiments showed that our content loss improves the faithful synthesis of low-dose images. Further, the performance of virtual contrast models increases if training data is extended by synthesized images from our GAN model trained by the noise-preserving content loss.

Acknowledgements

Thomas Pinetz and Alexander Efland are funded the German Research Foundation under Germany’s Excellence Strategy - EXC-2047/1 - 390685813 and - EXC2151 - 390873048. Robert Haase is funded by a research grant (BONFOR; O-194.0002.1).

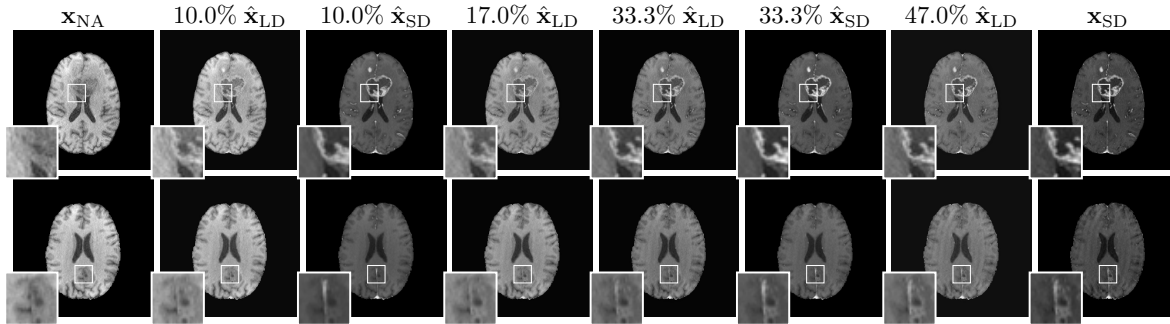


Figure 4: Comparison of synthesized LD images \hat{x}_{LD} and corresponding predicted SD images \hat{x}_{SD} for different dose levels on BraTS [37] along with the native (left) and real SD image (right). We also included non-fractional dosage levels (17% and 47%) to showcase the wide applicability of our algorithm. Top: the tumor is well contrasted in all \hat{x}_{SD} even for 10%. Bottom: the subtle enhancement of the tumor cannot be recovered from the 10% LD image.

References

- [1] ACR Manual on Contrast Media. American College of Radiology (2022)
- [2] Aja-Fernández, S., Vegas-Sánchez-Ferrero, G.: Statistical analysis of noise in MRI. Springer (2016)
- [3] Ammari, S., Bône, A., Balleyguier, C., Moulton, E., Chouzenoux, É., Volk, A., Menu, Y., Bidault, F., Nicolas, F., Robert, P., et al.: Can deep learning replace gadolinium in neuro-oncology?: a reader study. *Investigative Radiology* **57**(2), 99–107 (2022)
- [4] Arjovsky, M., Chintala, S., Bottou, L.: Wasserstein generative adversarial networks. In: ICML. pp. 214–223 (2017)
- [5] Kingma, D.P., Ba, J.: Adam: A method for stochastic optimization. In: ICLR (2015)
- [6] Armanious, K., Jiang, C., Fischer, M., Küstner, T., Hepp, T., Nikolaou, K., Gatidis, S., Yang, B.: Medgan: Medical image translation using gans. *Computerized Medical Imaging and Graphics* **79**, 101684 (2020)
- [7] Baid, U., Ghodasara, S., Mohan, S., Bilello, M., Calabrese, E., Colak, E., Farahani, K., Kalpathy-Cramer, J., Kitamura, F.C., Pati, S., et al.: The rsna-asnr-miccai brats 2021 benchmark on brain tumor segmentation and radiogenomic classification. *arXiv preprint arXiv:2107.02314* (2021)
- [8] Choi, Y., Uh, Y., Yoo, J., Ha, J.W.: Stargan v2: Diverse image synthesis for multiple domains. In: CVPR. pp. 8188–8197 (2020)
- [9] Gong, E., Pauly, J.M., Wintermark, M., Zaharchuk, G.: Deep learning enables reduced gadolinium dose for contrast-enhanced brain MRI. *Journal of Magnetic Resonance Imaging* **48**(2), 330–340 (2018)
- [10] Goodfellow, I., Pouget-Abadie, J., Mirza, M., Xu, B., Warde-Farley, D., Ozair, S., Courville, A., Bengio, Y.: Generative adversarial nets. In: Ghahramani, Z., Welling, M., Cortes, C., Lawrence, N., Weinberger, K. (eds.) *NeurIPS*. vol. 27. Curran Associates, Inc. (2014)
- [11] Gulrajani, I., Ahmed, F., Arjovsky, M., Dumoulin, V., Courville, A.C.: Improved training of wasserstein gans. *NeurIPS* **30** (2017)
- [12] Haase, R., Pinetz, T., Bendella, Z., Kobler, E., Paech, D., Block, W., Effland, A., Radbruch, A., Deike-Hofmann, K.: Reduction of gadolinium-based contrast agents in mri using convolutional neural networks and different input protocols: Limited interchangeability of synthesized sequences with original full-dose images despite excellent quantitative performance. *Investigative Radiology* (2023)
- [13] Haase, R., Pinetz, T., Kobler, E., Paech, D., Effland, A., Radbruch, A., Deike-Hofmann, K.: Artificial contrast: Deep learning for reducing gadolinium-based contrast agents in neuroradiology. *Investigative Radiology* (2023)
- [14] Ho, J., Jain, A., Abbeel, P.: Denoising diffusion probabilistic models. *NeurIPS* **33**, 6840–6851 (2020)
- [15] Isola, P., Zhu, J.Y., Zhou, T., Efros, A.A.: Image-to-image translation with conditional adversarial networks. In: CVPR. pp. 1125–1134 (2017)
- [16] Jacques, V., Dumas, S., Sun, W.C., Troughton, J.S., Greenfield, M.T., Caravan, P.: High relaxivity mri contrast agents part 2: Optimization of inner-and second-sphere relaxivity. *Investigative Radiology* **45**(10), 613 (2010)

- [17] Johnson, J., Alahi, A., Fei-Fei, L.: Perceptual losses for real-time style transfer and super-resolution. In: ECCV. pp. 694–711. Springer (2016)
- [18] Kanda, T., Ishii, K., Kawaguchi, H., Kitajima, K., Takenaka, D.: High signal intensity in the dentate nucleus and globus pallidus on unenhanced t1-weighted mr images: relationship with increasing cumulative dose of a gadolinium-based contrast material. *Radiology* **270**(3), 834–841 (2014)
- [19] Karras, T., Laine, S., Aila, T.: A style-based generator architecture for generative adversarial networks. In: CVPR. pp. 4401–4410 (2019)
- [20] Larsen, A.B.L., Sønderby, S.K., Larochelle, H., Winther, O.: Autoencoding beyond pixels using a learned similarity metric. In: ICML. pp. 1558–1566 (2016)
- [21] Lee, K., Chang, H., Jiang, L., Zhang, H., Tu, Z., Liu, C.: ViTGAN: Training GANs with vision transformers. In: ICLR (2022)
- [22] Liu, J., Pasumarthi, S., Duffy, B., Gong, E., Zaharchuk, G., Datta, K.: One model to synthesize them all: Multi-contrast multi-scale transformer for missing data imputation. arXiv preprint arXiv:2204.13738 (2022)
- [23] Lucic, M., Kurach, K., Michalski, M., Gelly, S., Bousquet, O.: Are gans created equal? a large-scale study. In: NeurIPS (2018)
- [24] Luo, H., Zhang, T., Gong, N.J., Tamir, J., Venkata, S.P., Xu, C., Duan, Y., Zhou, T., Zhou, F., Zaharchuk, G., Xue, J., Liu, Y.: Deep learning-based methods may minimize gbca dosage in brain mri. *European Radiology* **31**(9), 6419–6428 (2021)
- [25] Mao, X., Li, Q., Xie, H., Lau, R.Y., Wang, Z., Paul Smolley, S.: Least squares generative adversarial networks. In: ICCV. pp. 2794–2802 (2017)
- [26] Nie, D., Trullo, R., Lian, J., Petitjean, C., Ruan, S., Wang, Q., Shen, D.: Medical image synthesis with context-aware generative adversarial networks. In: MICCAI. pp. 417–425 (2017)
- [27] Pasumarthi, S., Tamir, J.I., Christensen, S., Zaharchuk, G., Zhang, T., Gong, E.: A generic deep learning model for reduced gadolinium dose in contrast-enhanced brain mri. *Magnetic Resonance in Medicine* **86**(3), 1687–1700 (2021)
- [28] Preetha, C.J., Meredig, H., Brugnara, G., Mahmutoglu, M.A., Foltyn, M., Isensee, F., Tobias, K., Pflüger, I., Schell, M., Neuberger, U., et al.: Deep-learning-based synthesis of post-contrast t1-weighted mri for tumour response assessment in neuro-oncology: a multicentre, retrospective cohort study. *The Lancet Digital Health* **3**(12), e784–e794 (2021)
- [29] Robic, C., Port, M., Rousseaux, O., Louguet, S., Fretellier, N., Catoen, S., Factor, C., Le Greneur, S., Medina, C., Bourrinet, P., Raynal, I., Idée, J.M., Corot, C.: Physicochemical and pharmacokinetic profiles of gadopipiclenol: a new macrocyclic gadolinium chelate with high t1 relaxivity. *Investigative Radiology* **54**(8), 475 (2019)
- [30] Ronneberger, O., Fischer, P., Brox, T.: U-net: Convolutional networks for biomedical image segmentation. In: MICCAI. pp. 234–241. Springer (2015)
- [31] Sauer, A., Schwarz, K., Geiger, A.: Stylegan-xl: Scaling stylegan to large diverse datasets. In: ACM SIGGRAPH. pp. 1–10 (2022)
- [32] Schieda, N., Blaichman, J.I., Costa, A.F., Glikstein, R., Hurrell, C., James, M., Jabehdar Maralani, P., Shabana, W., Tang, A., Tsampalieros, A., B. van der Pol, C., Hiremath, S.: Gadolinium-based contrast agents in kidney disease: a comprehensive review and clinical practice guideline issued by the canadian association of radiologists. *Canadian Journal of Kidney Health and Disease* **5** (2018)
- [33] Simonyan, K., Zisserman, A.: Very deep convolutional networks for large-scale image recognition. In: ICLR. pp. 1–14 (2015)
- [34] Wang, Z., Bovik, A.C., Sheikh, H.R., Simoncelli, E.P.: Image quality assessment: from error visibility to structural similarity. *Transactions on Image Processing* **13**(4), 600–612 (2004)
- [35] Xie, Y., Wang, X., Wang, R., Zha, H.: A fast proximal point method for computing exact wasserstein distance. In: Uncertainty in Artificial Intelligence. pp. 433–453 (2020)
- [36] Zhu, J.Y., Park, T., Isola, P., Efros, A.A.: Unpaired image-to-image translation using cycle-consistent adversarial networks. In: ICCV. pp. 2223–2232 (2017)
- [37] Baid, U., Ghodasara, S., Mohan, S., Bilello, M., Calabrese, E., Colak, E., Farahani, K., Kalpathy-Cramer, J., Kitamura, F.C., Pati, S., et al.: The rsna-asnr-miccai brats 2021 benchmark on brain tumor segmentation and radiogenomic classification. arXiv preprint arXiv:2107.02314 (2021)

Device	Male/Female	Weight	Field strength	Time to Echo	Repetition time	Flip angle	Resolution (mm)
Achieva	175/131	81.5 ± 18.3	3	3.1 ± 0.1	6.8 ± 0.1	8	$0.5 \times 0.5 \times 0.5$
Achieva	78/69	78.5 ± 17.1	1.5	3.3 ± 0.1	7.3 ± 0.1	8	$0.5 \times 0.5 \times 0.5$
Ingenia	22/7	90.3 ± 20.2	3.	3.8 ± 0.1	$7,7 \pm 0.1$	8	$0.5 \times 0.5 \times 1.0$
Ingenia	71/51	84.5 ± 19.3	1.5	3.6 ± 0.0	15.4 ± 0.04	30	$0.75 \times 0.75 \times 1.0$

Table 2: Details on the acquired data for this study

Supplementary material

Dataset Details

Our dataset consists of 453 studies, which were collected following approval by the Ethics Committee for Clinical Trials on Humans and Epidemiological Research with Personal Data of the Faculty of Medicine of the Rheinische Friedrich-Wilhelms-Universität Bonn (reference no. 450/20). Details are given in Table 2. Our training dataset uses a stratified split and consists of 50 patients with the following field strength and dose level combinations: 3T/0.1, 3T/0.2, 3T/0.33, 1.5T/0.2, and 1.5T/0.33. 10 patients are used to validate the algorithm and tune hyperparameters and the remaining 193 patients are used for testing. Additional 151 patients have been acquired at two different scanner to show the generalizability of our method and is detailed in Table 2. The preprocessing pipeline thereof is shown in Fig.6.

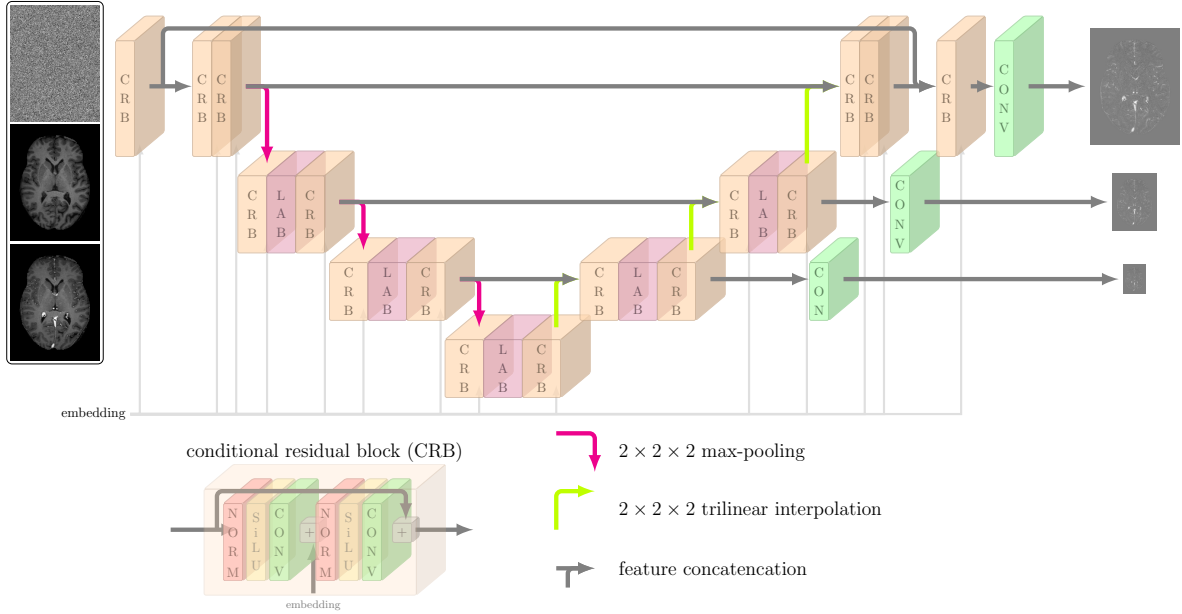


Figure 5: Architecture of the generator g_θ following a U-Net approach. At all four scales, conditional residual blocks (CRBs) are used to locally extract the contrast behavior from the native x_{NA} and standard-dose x_{SD} images.

Implementation Details

The architecture of the generator network g_θ is depicted in Figure 5 and is implemented using pytorch (1.13). At all four scales, conditional residual blocks (CRBs) are used to locally extract the contrast behavior from the native x_{NA} and standard-dose x_{SD} images. Every CRB receives a linear projection of an embedding that is generated by feeding the metadata into a two-layer neural network using 128 features. Every linear projection layer is learnable. At the finest scale, 12 feature channels are extracted, which are doubled after each max-pooling operation. The coarser scales additionally use local attention blocks (LABs) to aggregate local information within a $3 \times 3 \times 3$ search window using self-attention. All convolution layers utilize $3 \times 3 \times 3$ kernels.

As described in the paper, the discriminator f_ϕ implements the encoding side of the generator but used 5 scales and no LABs. The hyperparameters are identical to the generator.

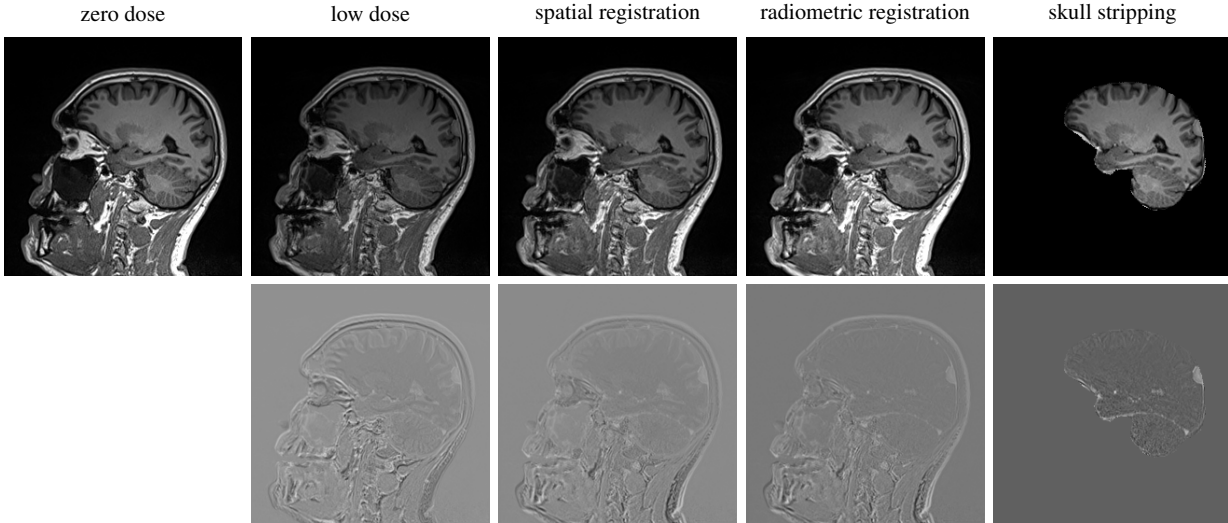


Figure 6: Visualization of the preprocessing steps. The top row shows the zero dose and the registration steps applied to a low-dose image. We adapt the preprocessing pipeline of BraTS [37], i.e, resampling, normalization, spatial registration, skull stripping, and radiometric registration. The bottom row illustrates the differences between the processed low-dose image and the zero dose.

Table 3: Ablation study between having shared or separate embeddings using PSNR, SSIM, and mean absolute error on contrast-enhanced regions (MAE_{CE}), and MAE of estimated standard deviations in non-contrast-enhanced regions (MAE_{σ}). p-values are computed using Wilcoxon signed rank test between GAN+VGG and GAN+Our.

Metric	Shared embeddings	Separate embeddings
PSNR	37.85	38.05
SSIM	0.975	0.976
MAE_{CE}	0.015	0.011 (p < 0.001)
MAE_{σ}	0.006	0.004 (p < 0.001)

To increase the receptive field of our noise-preserving loss ℓ_{NP} , we output multiple heads in the generator, see Figure 5. Then, ℓ_{NP} is computed in every scale using patches of size $n = 4$. For solving the Wasserstein problem, we perform 100 iterations of the inexact proximal point algorithm [35] to estimate the optimal transport map for every patch pair using the regularization parameter $\epsilon = \frac{\max(C)}{10}$.

For the optimization of the saddle point problem, the Adam [5] optimizer was used for both the generator g_{θ} and the discriminator f_{ϕ} with learning rates of 10^{-4} and momentum variables (0.5, 0.9). 5 discriminator updates are performed for each generator update. The training is performed for 100,000 iterations, with a minibatch size of 12 and a patch size of 64^3 on a A100 GPU with a runtime of 2 days and 13 hours. The weighting of the loss terms is independent of the used loss and we always set $\lambda_C = 1$ and $\lambda_{GAN} = 1$. The gradient penalty term λ_{GP} is set to 100 for stable training. For the virtual contrast model, the hyperparameters are taken from [27], with the only difference being the initial image size, which was set to 256 to reflect the changes in resolution from 0.5 mm to 1.0 mm. An ablation study on sharing the embedding between the generator and the discriminator is shown in Tab.3. Having a separate embedding for the discriminator and generator gives a slight performance improvement across all metrics. The p-values for the mean absolute error (MAE) in the contrast-enhanced regions (MAE_{CE}) and MAE of estimated standard deviations in non-contrast-enhanced regions (MAE_{σ}) indicate the difference is statistically significant.

Statistical evaluation of the contrast enhancement

In this section, the contrast enhancement of the generated images is statistically validated. For this reason, the CE pixels are extracted using the corresponding residual image of the standard-dose CE image toward the native image. For simplicity, we assume that every pixel that enhances at least by 10 % of our 0.95-quantile is contrast affected, while we consider the remainder as noise. The binary mask of CE pixels for a typical sample is illustrated in Figure 7. The contrast enhancement is then calculated using the mean over the CE pixels. Histograms of the mean absolute intensity errors in CE pixels (top) and the mean absolute standard deviation error in non-CE pixels (bottom) for the different

loss formulations are found on the left in Figure 8. The violin plots on the right illustrate the signal distribution in CE (top) and the standard deviations in non-CE (bottom) regions. The plots show that the contrast enhancement of our synthetic images better fits the ground truth low-dose images and the distribution of the contrast enhancements of our loss formulation better matches the ground truth than the other content loss formulations. The same observation holds for the standard deviation estimation in non-CE regions.

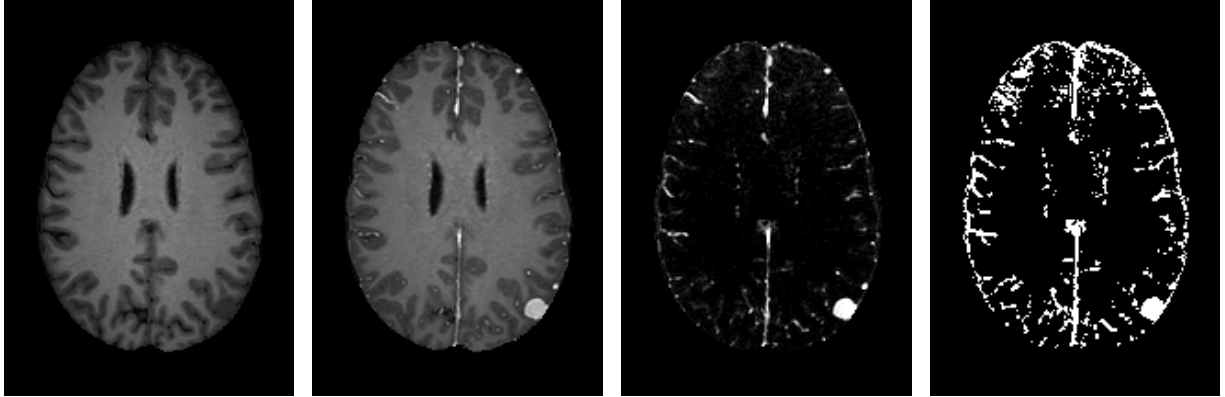


Figure 7: From left to right: native x_{NA} , standard dose x_{SD} , subtraction $x_{SD} - x_{NA}$ and the CE mask generated by thresholding the subtraction image by 0.1, which is equivalent to a 10% contrast increase compared to the 0.95-quantile of the native image x_{NA} .

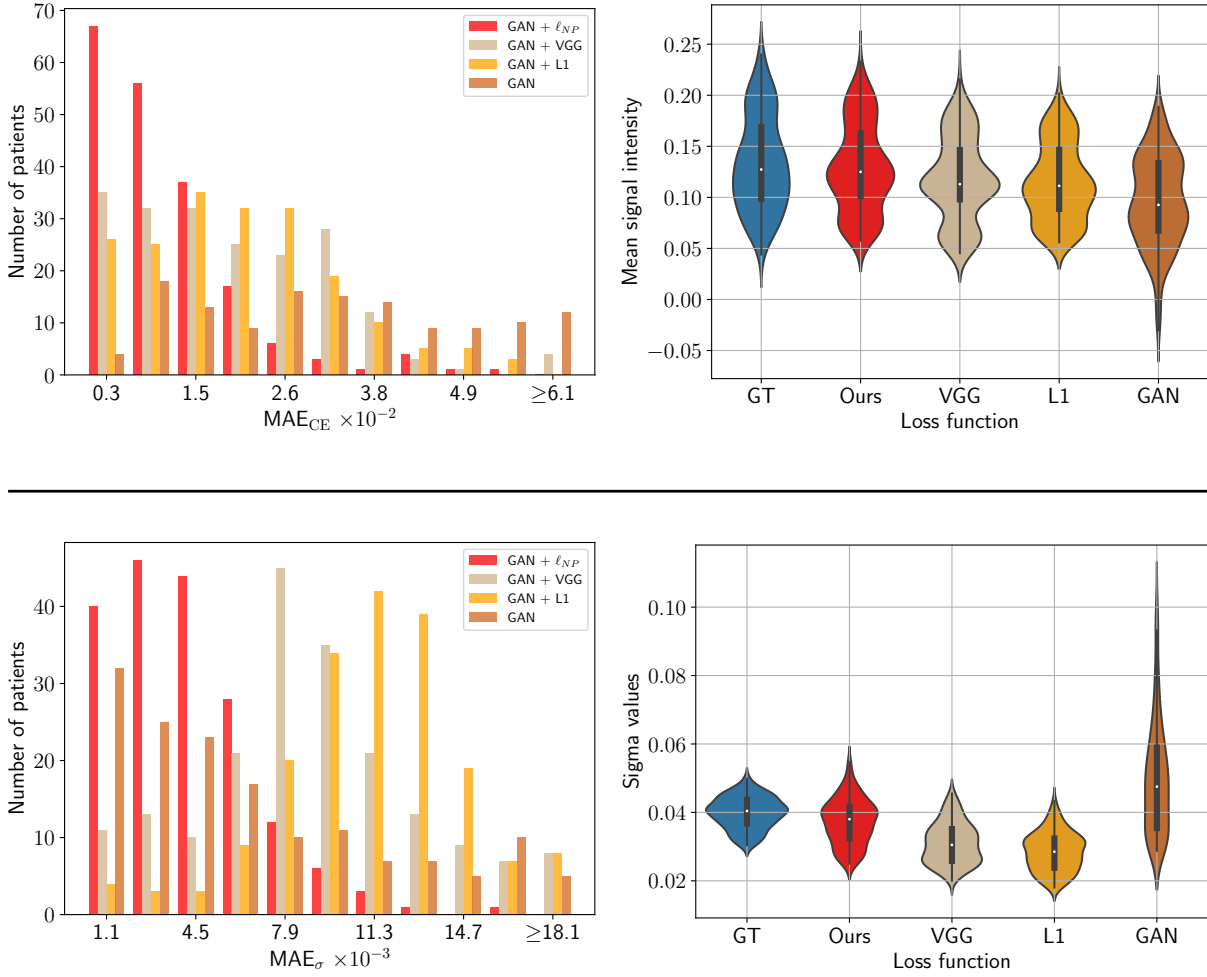


Figure 8: Statistical evaluation of contrast-enhancing regions (top) and non-enhancing regions (bottom). The histograms on the left compare the considered loss functions in both regions. While the top histogram shows the mean absolute error in the contrast signal, the bottom histogram visualizes the mean absolute error of the estimated standard deviations. The proposed noise preserving loss ℓ_{NP} has smaller densities at low errors in both metrics. The violin plots on the right illustrate how well the statistics within the CE region and non-CE regions overlap with the ground truth (GT). Comparing the different colored areas, we see that our distance function leads to the best overlap in both regions.